

# Spectra and Ionization Efficiencies of Charged Decay Particles in Kilonova Ejecta

Levi N. van den Berg,<sup>1,2,3\*</sup> Kenta Hotokezaka,<sup>2†</sup>

<sup>1</sup>*Institute for Theoretical Physics, Utrecht University, Princetonplein 5, 3584 CC Utrecht, The Netherlands*

<sup>2</sup>*Research Center for the Early Universe (RESCEU), Graduate School of Science, The University of Tokyo, 7-3-1 Hongo, Bunkyo, Tokyo 113-0033, Japan*

<sup>3</sup>*Department of Astronomy, Kyoto University, Kitashirakawa-Oiwake-cho, Sakyo-ku, Kyoto 606-8502, Japan*

Accepted XXX. Received YYY; in original form ZZZ

## ABSTRACT

Ionization by radioactive decay products including  $\alpha$ -particles,  $\beta$ -decay electrons, and fission fragments plays a central role in determining the nebular-phase ionization state and spectra of kilonovae. In this work, ionization cross sections, stopping powers, thermalization histories, and particle degradation spectra are calculated self-consistently for  $\alpha$ -particles and fission fragments propagating through expanding kilonova ejecta. The treatment includes interactions with bound and free electrons, charge evolution of fission fragments, adiabatic energy losses, and particle spectra obtained from the continuous slowing-down approximation and Spencer–Fano formalism. The work per ion pair is evaluated for a range of ejecta compositions and ionization states. Despite the large differences in mass, charge, and injection energy between  $\beta$ -electrons,  $\alpha$ -particles, and fission fragments, the resulting work per ion pair is found to be remarkably similar across all decay channels and target species considered. In particular, heavy-element ions exhibit nearly identical normalized ionization efficiencies for all decay products. This robustness arises because the ionization cross sections and stopping powers are governed by the same underlying collision physics, causing the ratio between ionization and energy loss to remain approximately constant over the relevant energy range. The results imply that the ionization state of late-time kilonova ejecta depends only weakly on the dominant radioactive decay channel, even in ejecta where  $\alpha$ -decay and fission dominate the heating budget.

**Key words:** neutron star mergers.

## 1 INTRODUCTION

Understanding the cosmic origin of the chemical elements requires studying astrophysical environments capable of producing nuclei heavier than lithium, which primordial nucleosynthesis cannot form (Peebles (1966); Wagoner et al. (1967)). Neutron-star mergers, observed as kilonovae, are leading candidates for sites of rapid neutron capture (the r-process, Burbidge et al. 1957; Cameron 1957; Lattimer & Schramm 1974 already hinted at by Alpher et al. 1948). Ejecta from these mergers could consist of components spanning a wide range of electron fractions ( $Y_e$ ) and velocities (e.g., Radice et al. 2018; Fujibayashi et al. 2023) that should give rise to different observational signatures (e.g., Kasen et al. 2017; Tanaka et al. 2018; Kawaguchi et al. 2024).

Spectroscopic study of the only gravitational-wave identified kilonova to date (AT2017gfo/GW170817) has revealed production of elements up to the light lanthanides and several trans-iron species (He I, Sr II, Y II, Te III, IV, La III, Ce III, in Watson et al. 2019; Domoto et al. 2022; Hotokezaka et al. 2023; Sneppen & Watson 2023; Sneppen et al. 2024b,a; Tanaka et al. 2023; Tarumi et al. 2023; Muhlolland et al. 2026; Chiba et al. 2026; Arya et al. 2026), yet no unambiguous detection of actinides or other very heavy r-process products

has been reported. Predictions for abundances beyond atomic numbers  $Z \gtrsim 98$  remain highly uncertain because of nuclear physics and mass-model differences that can change yields by orders of magnitude (for an overview, see Holmbeck et al. (2023)), while the lower-mass r-process pattern is constrained by observations of metal-poor stars (Burris et al. 2000). Signatures from long-lived heavy isotopes, for example spontaneous fission of  $^{254}\text{Cf}$ , can substantially modify kilonova light curves at tens to hundreds of days; detecting such signatures would provide direct evidence for synthesis of superheavy nuclei in merger ejecta (Wu et al. 2019a; Zhu et al. 2018). Measurements of radioactive isotopes in meteoritic and geological samples, such as Pu-244 and Cm-247, (Wallner et al. 2015, 2021; Tissot et al. 2016) further indicate r-process activity before solar-system formation and impose constraints on candidate astrophysical sites and timescales (Hotokezaka et al. 2015; Bartos & Marka 2019; Côté et al. 2019; Wehmeyer et al. 2023; Chiesa et al. 2024).

Previous studies of kilonova heating and late-time light curves have examined the energy deposition and thermalization of beta decay, alpha decay and fission, demonstrating that alpha decay and fission can dominate heating on  $\sim 10$ – $100$  day timescales (Barnes et al. 2016; Hotokezaka et al. 2016; Zhu et al. 2018; Wanajo 2018; Waxman et al. 2019; Wu et al. 2019a; Hotokezaka & Nakar 2020). Radioactive heating affects not only the kilonova luminosity but also the ionization state of the ejecta, which in turns determines the colour

\* E-mail: l.n.vandenberg@kustastro.kyoto-u.ac.jp

† E-mail: kentah@resceu.s.u-tokyo.ac.jp

evolution and strengths of absorption and emission lines (e.g., [Hotokezaka et al. 2021](#); [Pognan et al. 2023](#); [Brethauer et al. 2026](#); [Jerkstrand et al. 2026](#)). However, treatments of ionization and spectral effects have typically adopted ionization rates calibrated to beta decay products rather than to the heavier, more energetic particles produced by alpha decay and fission. Beta electrons carry decay energies that scale with parent lifetimes, while  $\alpha$ -particles and fission fragments are born with kinetic energies determined by quantum tunnelling and fragment dynamics. The energy scales relevant are a few MeV per nucleus for  $\alpha$ -particles and tens to hundreds of MeV for fission fragments ([Gamow 1928](#)). These higher energies, distinct stopping behaviours and different secondary cascade processes may change how decay energy thermalizes and how ionization proceeds within the ejecta.

This work derives ionization rates, stopping powers and particle spectra tailored specifically to  $\alpha$ -particles and fission fragments propagating in kilonova ejecta, accounting for their characteristic energies and interaction channels, including ionization of bound electrons, nuclear scattering and collective interactions with free electrons<sup>1</sup>. We couple these particle-specific thermalization rates to the late-time heating budget, quantifying how the partition of decay energy into heat and ionization differs from assumptions based solely on beta-decay products, where the novelty is in the self-consistent approach between thermalization and ionization cross sections. Using the degradation spectra for a given stopping medium, we compute the energy required to create an electron-ion pair referred to as the work per ion pair. We find that, for a plasma composed of r-process elements, the work per ion pair for  $\beta$  particles,  $\alpha$  particles, and fission fragments agrees to within  $< 50\%$ , demonstrating the robustness of the work per ion pair in the kilonova context. Furthermore, we provide an approximate formula to compute the work per ion for different ions. In Section 2 we develop the self-consistent framework needed to compute stopping powers and ionization cross sections for  $\alpha$ -particles and fission fragments, and use it to evaluate their thermalization. Section 3 introduces a prescription for their ionization efficiency and presents an analytic form for their instantaneous spectra. Section 4 extends this treatment to  $\beta$ -electrons by providing their spectra and ionization cross sections, enabling a direct and comprehensive comparison of ionization efficiencies across all charged decay products in neutron-star merger ejecta in section 5.

## 2 THERMALIZATION

Thermalization of decay products plays a critical role in determining the energy budget and ionization state of the kilonova ejecta. While the heating rate quantifies the initial energy deposition from fission and alpha decay fragments, not all of this energy contributes directly to ionization. The alpha and fission decay products lose their initial kinetic energy in roughly four channels: adiabatic expansion of the medium, collisions with free plasma electrons, collisions with electrons bound to plasma nuclei, and collisions with plasma nuclei themselves. Only the latter three are part of the thermalization. In addition, energy losses by collisions with plasma nuclei are negligible because of the positively charged nature of the decay products and the nucleus inducing a repulsive force which increases the size of the

<sup>1</sup> This all happens under the assumption that both fission and  $\alpha$ -particles are magnetically trapped, which seems to be the case as their respective Larmor radii are approximately  $10^{13}$  cm and  $10^{12}$  cm, for a relatively weak magnetic field of  $0.1 \mu\text{B}$  at 10 days, where the ejecta radius is  $10^{16}$  cm ([Waxman et al. 2019](#)).

impact parameter, thus decreasing the energy transfer efficiency. The relevant two channels are discussed below.

### 2.1 Stopping Power

The stopping power, or stopping force, describes the energy loss per unit track length for a particle travelling through a medium. It is defined by

$$-\frac{dE}{dx} = n \int_0^E E' \frac{d\sigma}{dE'} dE', \quad (1)$$

with  $d\sigma/dE$  the differential collision cross section for a single particle collision,  $n$  the number density of the medium,  $E'$  the energy lost in a collision, and  $E$  the kinetic energy of the decay product.

The stopping due to bound electrons can further be separated into two cases: projectile energy losses due to ionization and excitation. For the projectile velocities relevant here, the perturbation induced by the passing ion varies too rapidly for bound electrons to respond adiabatically. Electronic excitation, which requires a well-defined energy transfer matching a discrete transition, becomes unlikely because the interaction time is shorter than the characteristic timescales of bound-state dynamics. In contrast, ionization remains probable because the continuum of available final states does not impose such resonance conditions. Therefore, ionization overwhelmingly dominates the stopping power at these energies.

The differential cross section for such ionization events, derived under the assumption that the target mass is much smaller than the projectile mass, was formulated by [Gryziński \(1965a,b,c\)](#). The derivation is fully classical and treats the interaction as a binary collision between the projectile and a bound electron, with the binding energy entering only as a threshold condition on the energy transfer. The projectile is assumed to follow a straight-line trajectory, and the target electron is taken to be initially at rest apart from its binding energy. Under these assumptions, the energy transfer is obtained from classical scattering kinematics, leading to an analytic expression for the differential ionization cross section that depends only on the projectile velocity and the electron binding energy. The stopping power is given by

$$-\frac{dE}{dx} = n_i \sum_n N_n \frac{\pi (Z_n e^2)^2}{I_n} G_S(v_p/v_n), \quad (2)$$

where  $n_i$  denotes the ion density in the plasma, the index  $n$  sums over all electron orbitals of the target,  $N_n$  is the electron occupation number of said orbitals,  $Z_n$  is an effective charge of the projectile discussed later,  $e$  is the elementary charge,  $I_n$  the electron binding energy in orbital  $n$ ,  $v_p$  the projectile velocity,  $m_p$  the projectile mass and  $v_n = \sqrt{2I_n/m_e}$  the velocity of the bound electron with  $m_e$  the electron mass. The velocity matching function  $G_S$  is defined by

$$G_S(V) = \begin{cases} f_1(V) f_2(V) f_3(V), & V > 0.243, \\ \frac{128}{45} V^4, & V \leq 0.243, \end{cases} \quad (3)$$

with

$$\begin{aligned} f_1(V) &= \frac{V}{(1+V^2)^{3/2}}, \\ f_2(V) &= \frac{m_e/m_p}{1+V^2} \log(\alpha) + \frac{4}{3} \left(1 - \frac{1}{\alpha}\right) \log(2.7+V), \\ f_3(V) &= 1 - \alpha^{-(1+V^2)}. \end{aligned}$$

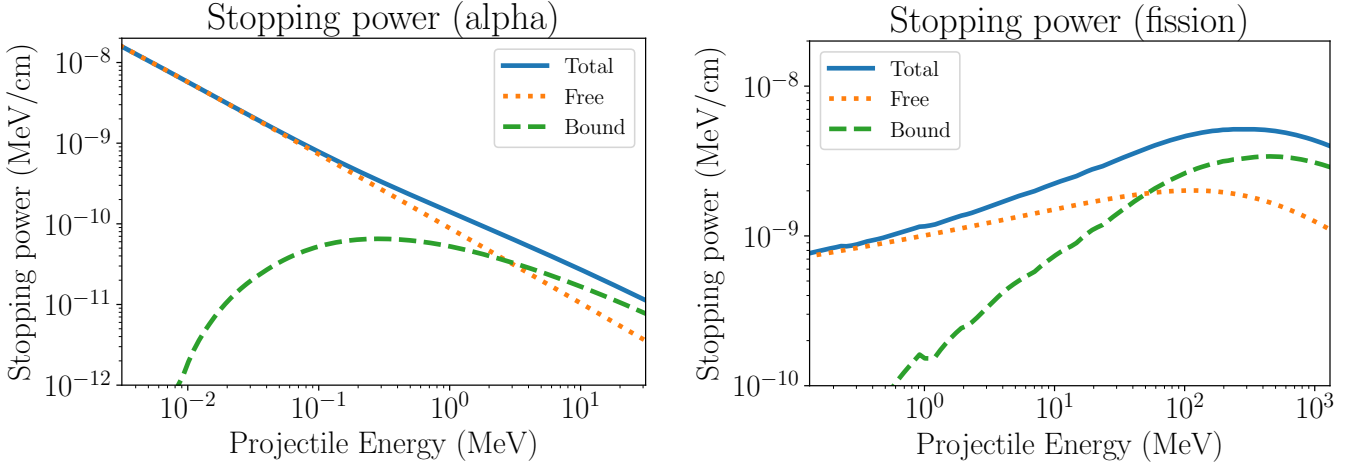


**Figure 1.** Stopping power contributions from free and bound electrons for xenon fission fragments and  $\alpha$ -particles propagating through a Xe II plasma with  $n_e = n_i = 10^{10} \text{ cm}^{-3}$ . For the fission fragment, the effective charge  $Z_{\text{eff}}$  is taken from the equilibrium values given by Eq. 5, while  $Z_{\text{eff}} = 2$  is adopted for the  $\alpha$ -particles.

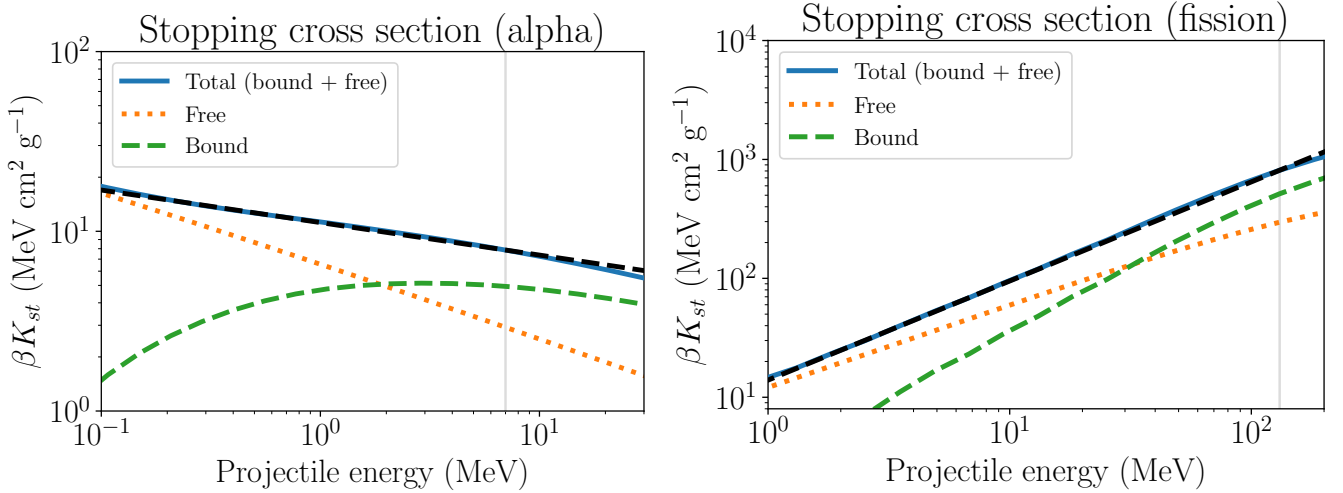


**Figure 2.** Same configuration as in Fig. 1. The stopping cross sections  $\beta K_{st}$ , with  $\beta = v/c$ . An additional dashed black line has been drawn to illustrate the power law behaviour  $\propto E^\alpha$ , with  $\alpha \approx 1.0$  for fission, and  $\alpha \approx -0.2$  for  $\alpha$ -particles. Typical injection energies for fission and  $\alpha$ -particles have been indicated with a gray line at  $E_0 \approx 130$  and  $E_0 \approx 7$  MeV for fission and alpha respectively.

where  $\alpha = 4V(1+V)$  and the value of  $V \approx 0.243$  makes the piecewise function continuous.

To obtain consistent and shell-resolved electron binding energies for the ionization model, atomic structure calculations are performed using the PySCF package (Sun et al. 2018). All calculations employed the relativistic X2C Hamiltonian together with the all-electron x2c-QZVPPa11 basis set, which provides high-quality orbital energies suitable for use as binding energies in the stopping-power calculations. Using these binding energies, the stopping powers calculated for a neutral xenon target gas agree with the tabulated values in the NIST ASTAR database (Berger et al. 2005) within the energy interval relevant for thermalization.

For the contribution to the projectile stopping due to free plasma electrons, another approach is taken. Since the electron temperature in the nebular phase of the merger ejecta has dropped significantly, the velocity of the fission and alpha fragments far exceeds that of thermal electrons. In this regime, the stopping power due to thermal

electrons is given by the Bohr formula (Bohr 1913):

$$-\frac{dE}{dx} = \left( \frac{Z_{\text{eff}} e \omega_p}{v_p} \right)^2 \ln \left( \frac{m_e v_p^3}{Z_{\text{eff}} e^2 \omega_p} \right), \quad (4)$$

where  $Z_{\text{eff}}$  is the effective projectile charge,  $e$  the elementary charge,  $v_p$  the projectile velocity,  $m_e$  the electron mass, and  $\omega_p$  the electron plasma frequency  $\omega_p = \sqrt{4\pi n_e e^2 / m_e}$ , with  $n_e$  the free-electron density. The total stopping power is then obtained by summing the contributions from bound and free electrons.

## 2.2 Effective charge

Only the effective projectile charge remains to be determined in the stopping power for fission and alpha decay particles. Particular care must be taken when analysing the thermalization of fission fragments, as they retain bound electrons, whereas  $\alpha$ -particles remain

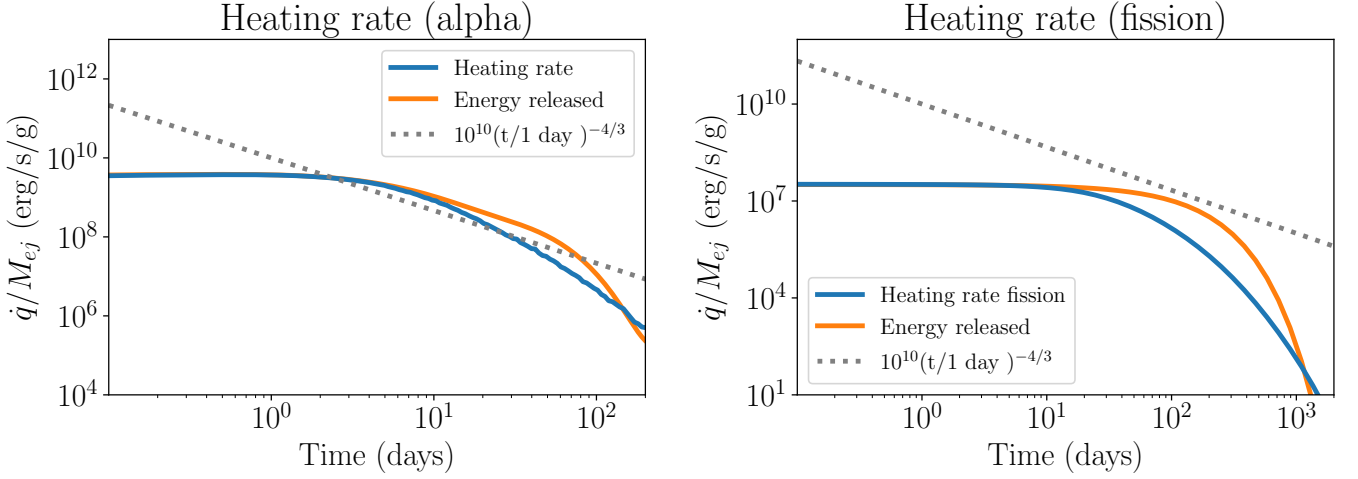


**Figure 3.** Plots of the heating rate (blue) found for fission fragments and alpha decay particles normalized by the ejecta mass  $M_{ej} = 0.05M_{\odot}$ , compared to the respective decay energy released per unit time (orange). Initial abundances for alpha decay are  $Y(\text{Rn-222}) = 4.0 \times 10^{-5}$ ,  $Y(\text{Ra-223}) = 2.7 \times 10^{-5}$ ,  $Y(\text{Ra-224}) = 4.1 \times 10^{-5}$  and  $Y(\text{Ra-225}) = 2.7 \times 10^{-5}$ . For spontaneous fission an abundance  $Y(\text{Cf-254}) = 2.0 \times 10^{-6}$  has been placed. All abundances are taken from [Wu et al. \(2019b\)](#). The dashed grey line represents the analytical heating rate by beta decay.

fully ionized. At velocities relevant to this context, charge transfer is the primary mechanism for increasing the number of bound electrons, while single ionization serves as the dominant process for their reduction. Using the charge change rates obtained in [Peter & Meyer-ter Vehn \(1991a\)](#), it becomes clear that the thermalization rate defined as  $\alpha_{th} = d \ln(E)/dt$  is approximately four orders of magnitude smaller than the capture and ionization rate. The consequence of this, is that the effective charge of the fission fragment acts as an evolution along equilibrium values from the charge rates, and is therefore well approximated by [Schwartz & Grande \(2001\)](#). The fit-formula is given as

$$Z_{eff} = Z_p \frac{376x + x^6}{1428 - 1206x^{0.5} + 690x}, \quad (5)$$

with

$$x = \left( \frac{v_p}{v_0} Z_p^{-0.52} Z_t^{0.03-0.017Z_p^{-0.52}v_p/v_0} \right)^{1+0.4/Z_p}, \quad (6)$$

with  $Z_p$  the proton number of the projectile atom, and  $Z_t$  the proton number of the target atoms.

### 2.3 Expanding Medium

In addition to the loss of energy via collisions, the particles travel in an expanding medium and therefore lose energy via adiabatic expansion. The energy loss rate for a sub-relativistic projectile is given by

$$\frac{dE}{dt} = -\frac{3(\gamma-1)U}{t} - \left( v \frac{dE}{dx} \right)_{plasma}. \quad (7)$$

The energy loss rate by plasma collisions can be written in the form

$$\left( \frac{dE}{dt} \right)_{plasma} = \left( v \frac{dE}{dx} \right)_{plasma} = -v\rho_m(t)K_{st}(t, v), \quad (8)$$

by the introduction of a stopping cross section  $K_{st}(t, v) = K_{st,free}(t, v) + K_{st,bound}(t, v)$  and a mass weight density  $\rho_m = C_p M_{ej} t^{-3} v_0^{-3} = \rho_0 t^{-3}$ , with  $C_p$  a normalization constant under the

assumption of a power law mass density profile ([Hotkezaka & Nakar 2020](#)).

As shown in Fig. 2, the stopping power follows a power law in energy for velocities relevant for thermalization. Because of this, Eq. 8 is well approximated by the following

$$\left( \frac{dE}{dt} \right)_{plasma} = -\rho_m(t) \left[ v K_{st}(t, v) \Big|_{t=t_0} \right] \left( \frac{E}{E_0} \right)^{\alpha}, \quad (9)$$

where  $t_0$  is the time at which a fission or alpha decay fragment is released with an initial energy  $E_0$  and  $\alpha$  is the power-law index. For the complete energy evolution, a term  $-2E/t$  accounting for adiabatic energy losses from the expanding medium should be added. This results in a Bernoulli type differential equation and has an analytical solution

$$E(t, t_0, E_0) = \left( E_0^{1-\alpha} \left( \frac{t_0}{t} \right)^{2(1-\alpha)} + \frac{(\alpha-1)\rho_0(vK_{st})_0 E_0^{-\alpha} \left[ \left( \frac{t}{t_0} \right)^{2\alpha} - 1 \right]}{2\alpha t^2} \right)^{1/(1-\alpha)}. \quad (10)$$

By means of Eq. 10 the kilonova heating rate at a time  $t$ , as done by a single decay product emitted at a time  $t_0$  is given by

$$\begin{aligned} \dot{q}_i(t, t_0) &= \rho_m(t) v K_{st}(t, E(t, t_0, E_{0,i})) \\ &= \rho_m(t) \sqrt{\frac{2E(t, t_0, E_{0,i})}{m_p}} K_{st}(t, E(t, t_0, E_{0,i})). \end{aligned} \quad (11)$$

Approximating the radioactive decay rate of a nucleus as  $\dot{N}_i \approx N_i/\tau_i$ , where  $\tau_i$  is the nucleus lifetime. For alpha decay in particular, decay chains have to be taken into account, here only dominant decay modes are considered and obtained from [International Atomic Energy Agency \(2025\)](#). The evolution of abundances are given by the Bateman equations ([Bateman 1910](#)). The total heating rate at a time  $t$  is then given by ([Hotkezaka & Nakar 2020](#))

$$\dot{q}(t) = \sum_i \int_{t_{0,i}}^t dt_0 \dot{q}_i(t, t_0) \frac{N_i(t_0)}{\tau_i}, \quad (12)$$

where  $t_{0,i}$  is the time at which particles that are not thermalized at time  $t$  are synthesized. Figure 3 shows the heating rates of fission and alpha decay, which is in accordance with [Hotokezaka & Nakar \(2020\)](#) despite the difference of the stopping power models used.

### 3 IONIZATION FOR ALPHA AND FISSION

Ionization processes in plasmas are governed by the interaction between energetic particles and bound electrons. The probability of ionization is quantified by the ionization cross section, which depends on the projectile's effective charge and velocity relative to the electron's orbital motion. To translate this microscopic interaction into macroscopic ionization rates, one must consider the particle energy spectrum, which describes how charged particles lose energy as they traverse a medium. This spectrum is shaped by both collisional losses and the injection profile of the particles, and is formally described by the Spencer–Fano equation.

#### 3.1 Ionization Cross Section and Instantaneous Spectrum

The ionization cross section for an electron in the  $n$ th shell follows directly from the differential ionization cross section introduced earlier in the context of the stopping power. Integrating the differential expression over all allowed energy transfers gives

$$\sigma_{\text{ion},n}(v_p) = \int_0^{E(v_p)} \frac{d\sigma_n}{dE'} dE' = \pi \left( \frac{Z_n e^2}{I_n} \right)^2 G \left( \frac{v_p}{v_n} \right), \quad (13)$$

where  $Z_n$  denotes the effective charge experienced by the electron in orbital  $n$ ,  $e$  is the elementary charge,  $I_n$  the corresponding binding energy, and  $G$  the corrected velocity-matching function that relates the projectile velocity  $v_p$  to the characteristic orbital velocity  $v_n$ . This provides a self-consistent description of the stopping and ionization process needed to guarantee the accuracy of the ionization efficiency. The corrected velocity matching function is defined as ([McGuire & Richard 1973](#))

$$G(V) = \begin{cases} g_1(V) g_2(V) g_3(V), & V > 0.215, \\ \frac{4}{15} V^4, & V \leq 0.215, \end{cases} \quad (14)$$

with

$$g_1(V) = \frac{\alpha^{3/2}}{V^2}, \quad (15)$$

$$g_2(V) = (1 - \beta) (1 - \beta^{1+V^2}), \quad (16)$$

$$g_3(V) = \alpha + \frac{2}{3} (1 + \beta) \ln(2.7 + V), \quad (17)$$

where the parameters  $\alpha$  and  $\beta$  are defined as

$$\alpha = \frac{V^2}{1 + V^2}, \quad \beta = \frac{1}{4V(1 + V)}. \quad (18)$$

The screened or effective projectile charge that is presented in Eqs. 2 and 13 can be constructed by solving for the number of electrons inside a spherical volume of radius  $b_n = \sqrt{\sigma_{\text{ion}}/\pi}$ , as is done in [Peter & Meyer-ter Vehn \(1991b\)](#):

$$\begin{cases} Z_n = Z_p - \sum_{n'} N_{n'} \int_0^{b_n} d^3\mathbf{r} |\psi_{n'}(\mathbf{r})|^2, \\ Z_n = \frac{I_n b_n}{e^2 \sqrt{G(v_p/v_n)}}. \end{cases} \quad (19)$$

The normalized wave function of each orbital  $\psi_n$  is obtained from the same PySCF calculations used to determine the binding energies, guaranteeing internal consistency between the orbital shapes and their corresponding energies.

The construction of the ionization rate from the particle degradation spectrum has been explored in several early studies, including the influential treatment by [Axelrod \(1980\)](#) in the context of radioactive energy deposition in supernovae ejecta. In the case of heavy and sub-relativistic particles, the energy loss per collision compared to the kinetic energy is substantially reduced in comparison to beta electrons. The energy spectrum of a charged particle slowing down in a medium is determined by the balance between collisional energy losses and the injection of new particles from a source. [Spencer & Fano \(1954\)](#) derived an integral equation that captures this balance in steady state, now known as the *integral form of the Spencer-Fano equation*:

$$y(E) \int_0^E d\epsilon k(E, \epsilon) = \int_0^\infty d\epsilon y(E + \epsilon) k(E + \epsilon, \epsilon) + s(E), \quad (20)$$

where  $s(E)$  denotes the source term, representing a uniformly distributed number of particles injected per unit volume, time, and energy ( $\text{cm}^{-3} \text{s}^{-1} \text{erg}^{-1}$ ). The function  $k(E, \epsilon) d\epsilon$  gives the probability per unit path length ( $\text{cm}^{-1}$ ) that a particle of energy  $E$  loses an amount  $\epsilon$ . Finally,  $y(E)$  is the particle energy spectrum, expressed as flux per unit energy ( $\text{cm}^{-2} \text{s}^{-1} \text{erg}^{-1}$ ). The stopping power is then defined as

$$S(E) = \int_0^E d\epsilon \epsilon k(E, \epsilon). \quad (21)$$

For a mono-energetic source, the function takes the form  $s(E) = s_0 \delta(E - E_0)$ , where  $s_0$  is the source strength ( $\text{cm}^{-3} \text{s}^{-1}$ ). Introducing a normalized spectral function  $\bar{y}(E) \equiv y(E)/s_0$  with units  $\text{cm erg}^{-1}$ , the Spencer-Fano equation becomes

$$\bar{y}(E) \int_0^E d\epsilon k(E, \epsilon) = \int_0^\infty d\epsilon \bar{y}(E + \epsilon) k(E + \epsilon, \epsilon) + \delta(E - E_0). \quad (22)$$

The maximum energy transfer in a collision with an electron is  $2m_e v_p^2$ , which is much smaller than the kinetic energy of a fission fragment or  $\alpha$ -particle, scaling as  $m_e/m_p \ll 1$ . Consequently,  $k(E, \epsilon)$  has support only for  $\epsilon \ll E$ . Expanding Eq. 22 under this assumption, and introducing a cut-off  $\epsilon \ll \epsilon' \ll E$ , yields

$$\begin{aligned} \bar{y}(E) \int_0^{\epsilon'} d\epsilon k(E, \epsilon) &\approx \int_0^{\epsilon'} d\epsilon \left[ \bar{y}(E) k(E, \epsilon) \right. \\ &\quad + \bar{y}(E) \frac{\partial k(E, \epsilon)}{\partial E} \epsilon \\ &\quad \left. + k(E, \epsilon) \frac{\partial \bar{y}(E)}{\partial E} \epsilon \right] + \delta(E - E_0). \end{aligned} \quad (23)$$

For  $E \neq E_0$ , the solution is simply

$$\bar{y}(E) \approx \left( \int_0^{\epsilon'} d\epsilon \epsilon k(E, \epsilon) \right)^{-1} = \frac{1}{S(E)}. \quad (24)$$

Having established the form of the energy spectrum, the number of ionizations  $N_i$  can be determined directly. Since  $\bar{y}(E)$  describes the effective path length of a particle with energy  $E$ , and given the ion number density  $n_{\text{ion}}$  and ionization cross section  $\sigma_{\text{ion}}(E)$ , the ionization yield is

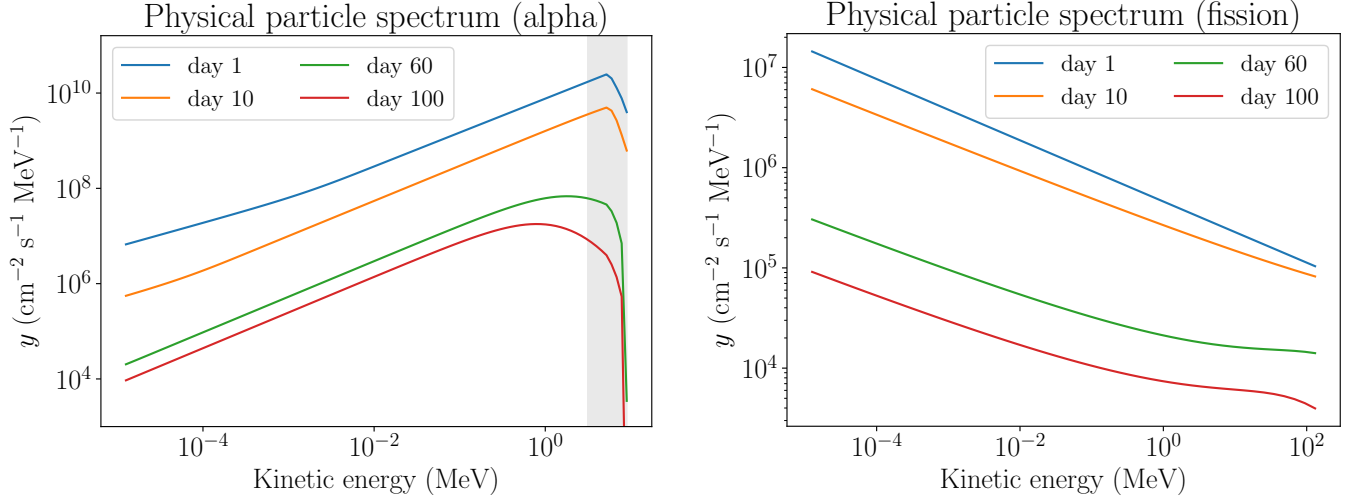


**Figure 4.** Particle spectra for fission and  $\alpha$ -particles coming from the same ejecta configuration as Fig. 3. For the alpha case, the kinetic energy range of  $\alpha$ -particles is represented by the gray area, with larger decay energies being many times more numerous at the given times.

$$N_i = \int_{E_{\text{th}}}^{E_{0,i}} dE n_{\text{ion}} \sigma_{\text{ion}}(E) \bar{y}(E), \quad (25)$$

where  $E_{\text{th}}$  is the thermalization energy of the projectile.

It should be noted that this expression accounts only for primary ionizations. In reality, additional ionizations occur due to secondary electrons liberated in the process. For fission fragments, these secondary electrons have kinetic energies in the range  $E_{\text{min}} \approx 250 \text{ eV} < E_s < E_{\text{max}} \approx 200 \text{ keV}$ , where  $E_{\text{min}}$  is set by the minimum Coulomb energy transfer and  $E_{\text{max}}$  by the kinematic limit, and strongly dominated by the lower energy tail. In the present work, we therefore safely neglect any contributions from these secondary electrons for the ionizing fission fragments and  $\alpha$ -particles.

### 3.2 Physical Particle Spectrum

In the previous case, the degradation spectrum for fission and  $\alpha$ -particles describes the steady-state number of particles that travel through the medium. There is no notion of adiabatic expansion. Since thermalization is described via the continuous slowing down approximation, the construction of a continuity equation is permitted. The goal is to obtain a single-particle spectrum, meaning the energy evolution of a particle is only time dependent. The continuity equation is given by

$$\frac{dN}{dt} + N \frac{\partial \dot{E}}{\partial E} = Q, \quad (26)$$

where the particle spectrum  $N(E, t)$  denotes the number of particles per unit energy, and the source term  $Q(E, t)$  denotes the number of particles produced by decay per unit energy per unit time (for exponential decay this is just  $\exp(-t/\tau)/\tau$ ). Since the decays discussed are only mono-energetic, the source term is given by  $Q(E, t) = \dot{N}_{inj} \delta(E(t) - E_0)$ , where  $\dot{N}_{inj}$  is the number of particles that are released by a decay at time  $t_0$ . Since Eq. 26 is a linear

first order ordinary differential equation, the solution is given by

$$N(E, t) = \frac{\dot{N}_{inj}(t_0)}{\|\dot{E}(E_0, t_0)\|} \exp\left\{-\int_{t_0}^t \left(\frac{\partial \dot{E}}{\partial E}\right) dt'\right\} = \frac{\dot{N}_{inj}(t_0)}{\|\dot{E}(E_0, t_0)\|} \times \exp\left\{\int_{t_0}^t \left(\frac{2}{t'} + \alpha \rho_m(t') \left[v K_{st}(t, v)\right]_{t=t_0}\right) (E(t'))^{\alpha-1} E_0^{-\alpha} dt'\right\}. \quad (27)$$

Using the power-law approximation for the stopping power—which remains valid over many orders of magnitude below the kinetic energy set by the decay—and including adiabatic expansion losses, the energy evolution follows Eq. 10. Finally, because the particles move along a trajectory and strictly decrease in energy, there is a one-to-one correspondence to be made between a particles current energy  $E(t)$  and the time  $t_0$  when it entered the medium. This relation must be numerically inverted to obtain  $N(E, t)$  instead of  $N(t_0, t)$ . The presented integral has to be performed numerically.

The physical spectra for fission and  $\alpha$ -particles are presented in Fig. 4, where the spectrum  $y(E, t) = n(t)v(E)N(E, t)$ , with  $v$  being the speed of the fission or  $\alpha$ -particles and  $n$  denotes the number density of the parent nucleus responsible for this decay in the ejecta. The spectra exhibit clear transitions between physical regimes. At early times, the ejecta density is high and collisional energy loss dominates. Under these conditions, decay products thermalize on timescales much shorter than the dynamical time of the ejecta, and the spectra reduce to the instantaneous form of Eq. 24. At later times, however, the ejecta has expanded and its density has dropped substantially. Adiabatic losses then become the dominant energy-loss channel, and decay products require much longer to thermalize.

This behaviour imprints itself on the spectra. The low-energy portion (below  $\sim 0.1 \text{ MeV}$ ) is populated mainly by particles produced around  $\sim 20$  days after merger, when collisional losses still shaped the spectrum; adiabatic expansion alone introduces no structure because it scales linearly with kinetic energy. At higher energies, the spectrum flattens at late times due to the dominance of adiabatic cooling. This flattening is partially masked by the exponential decay of the parent nuclei, which suppresses the high-energy end of the spectrum at late times.

Target	WIP
Xe I	2.6/2.5
Xe II	6.7/6.5
Xe III	8.8/8.5
Xe IV	14.3/13.6
Xe V	18.1/16.9

(a) Xenon charge states

Target/Medium	He I	He II	Sr II	Xe II	Nd II
He I	2.3/2.3	11.7/11.7	20.6/20.6	23.1/22.7	24.8/24.4
He II	13.0/12.6	30.1/28.9	53.9/51.8	60.7/57.4	65.2/61.6
Sr II	2.4/2.4	8.0/8.1	14.2/14.3	16.0/15.7	17.1/16.9
Xe II	0.9/0.9	3.6/3.3	6.0/5.9	6.7/6.5	7.2/7.0
Nd II	1.2/1.2	4.1/4.2	7.2/7.3	8.1/8.1	8.9/8.7

(b) Work per ion pair for various media

**Table 1.** Work per ion pair for fission fragments and alpha-particles (fission WIP/alpha WIP). Table 1a shows results for neutral ejecta composed solely of xenon in different charge states, and thermal electrons with abundance fractions  $\chi_e = 0, 1, 2, 3, 4$  from top to bottom. Table 1b shows results for various media, where particle spectra are generated using collisions with the listed ions but ionization cross sections are substituted from other species. We adopt  $\chi_e = 0.1$  for He I and  $\chi_e = 1$  otherwise. All values are in units of  $I$ .

### 3.3 Ionization Efficiency

With the results from the previous two sections, a measure for the ionization efficiency can be computed, with the work per ion pair being defined as

$$w_i = \frac{E_{0,i}}{N_i}. \quad (28)$$

For fission fragments and  $\alpha$ -particles, we find values for the work per ion pair between  $w = 2.5I$  and  $w = 18.1I$  for Xe I and Xe V respectively (see Table 1a), where  $I$  is the ionization potential of the most loosely bound electron. Here, the ejecta are assumed to be quasi-neutral and consist only of thermal electrons and one of the xenon-ion species. We note that the work per ion value for alpha decay particles in a Xe I gas is consistent with experiments recorded in the literature (Giesen & Beck 2014; Baek & Grosswendt 1995).

In Table 1b, we show work per ion pair for cases in which the particle spectra of fission fragments and  $\alpha$ -particles are fixed by the indicated medium, while the ionization cross sections are substituted with those of other ions. The various media are He I with an electron abundance fraction  $\chi_e = 0.1$ , and for He II, Sr II, Xe II and Nd II we fixed  $\chi_e = 1$ . The results again show no significant difference in ionization efficiency between  $\alpha$ -particles and fission fragments. Both projectiles follow the same underlying physics and are far more massive than the bound and free electrons they ionize, leading to nearly identical work per ion pair. In general,  $\alpha$ -particles appear slightly more efficient, a consequence of treating their charge as a constant +2, whereas fission fragments undergo charge evolution and a slight increase in typical initial kinetic energy over fission fragments.

## 4 IONIZATION AND SPECTRUM FOR $\beta$ -ELECTRONS

In contrast to heavy charged particles, the transport and thermalization of  $\beta$ -electrons in kilonova ejecta have been studied extensively (Barnes et al. 2016; Waxman et al. 2019; Kasen & Barnes 2019; Hotokezaka & Nakar 2020), and their role in powering the light curve is comparatively well understood. Most existing work, however, focuses on their heating efficiency rather than their detailed spectral evolution or ionization behaviour. To place our heavy-particle results in context, we therefore also examine the  $\beta$ -electron spectrum and its associated work per ion pair.

For the  $\beta$ -electron spectrum, the same principles apply as for the fission and  $\alpha$ -particles, though the degradation of the electrons occurs

through a wider selection of channels. The degradation equation is

$$\begin{aligned} \bar{y}(E) \int_{\epsilon_0}^E k(E, \epsilon) d\epsilon = & \sum_n \bar{y}(E + \epsilon_n) k_n(E + \epsilon_n, \epsilon_n) \\ & + \sum_{\alpha} \int_{I_{\alpha}}^{\lambda_{\alpha}} \bar{y}(E + \epsilon) k_{\alpha}(E + \epsilon, \epsilon) d\epsilon \\ & + \sum_{\alpha} \int_{2E+I_{\alpha}}^{E_0} \bar{y}(E') k_{\alpha}(E', E + I_{\alpha}) dE' \\ & + \sum_{\alpha} \eta_{\alpha} \delta(E - \epsilon_{\alpha}) \int_{I_{\alpha}}^{E_0} \bar{y}(E') \sigma_{\alpha}(E') dE' \\ & + \frac{d}{dE} [L_{\text{th}}(E) \bar{y}(E)] + \delta(E - E_0). \quad (29) \end{aligned}$$

where  $\epsilon_n$  is excitation energy and  $I$  is the ionization potential, and  $\lambda_{\alpha} = \min(E_0 - E, E_{\alpha} + I)$ . The first and second terms of the right-hand side of equation (29) correspond to the probability of the enter of electrons with  $T' > T$  to  $(T, T + dT)$  by excitation and ionization, respectively. The third term describes the generation of secondaries in  $(E, E + dE)$ . The fourth term accounts for the production of Auger electrons following inner shell ionization, where the ionization of the  $\alpha$ th shell is followed by an Auger electron of energy  $\epsilon_{\alpha}$  is created with a probability  $\eta_{\alpha}$ . The fifth term is the energy loss due to Coulomb collision with thermal electron (see Kozma & Fransson 1992, for  $L_{\text{th}}$ ). In ionized medium  $\chi_e \gtrsim 1$ , the contributions of excitation and Auger electrons are less than 10%, and therefore, we neglect these in this work. The ionization cross sections by electron impacts are computed by using HULLAC (Bar-Shalom et al. 2001). The energy distribution of secondary electrons is assumed as (Opal et al. 1971)

$$P(E_p, E_s) = \frac{1}{\text{Jarctan}((E_p - I)/J)} \frac{1}{1 + (E_s/J)^2}, \quad (30)$$

where  $E_p$  and  $E_s$  are the primary and secondary energy, and  $I$  is the ionization potential of the shell, and we use  $J = 0.7I$  (Kozma & Fransson 1992).

Figure 5 shows the electron degradation spectra in pure Xe medium with an initial kinetic energy of beta-particle of  $E_{\beta} = 300$  keV. The spectra for  $\chi_e = (0.1, 1, 2, 3, 4)$  correspond to the medium composed of Xe I, Xe II, Xe III, and Xe IV, respectively. For  $E \gtrsim E_{\beta}/3$ , the electron spectra are proportional to the reciprocal of the stopping powers same as the cases for heavy particle. In the lower energy regime,  $E \lesssim E_{\beta}/3$ , the contribution of secondary electrons significantly increases the flux. The flux at lower energies decreases with increasing the electron fraction because the stopping due to the Coulomb collision is more efficient for higher  $\chi_e$ . The ionization due to secondary electrons increases the ionization rates by a factor of 2–3.

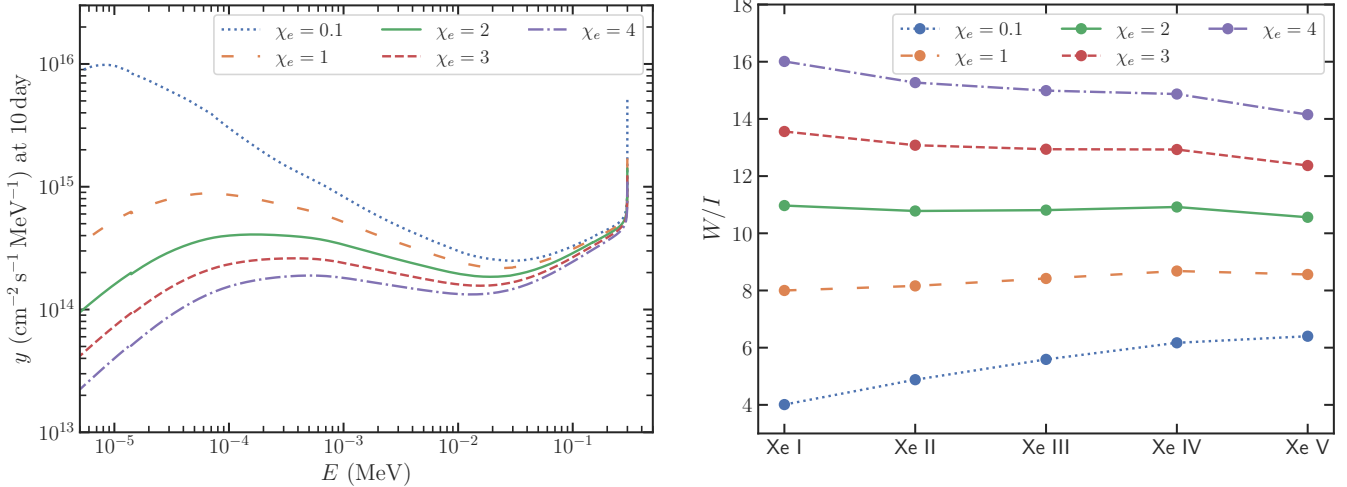


**Figure 5.** Electron spectra (*left*) for the same ejecta configuration as Fig. 3. Work per ion pair for  $\beta$ -electrons and their secondaries for different ionization stages of xenon (*right*).

Target/Medium	He I	He II	Sr II	Xe II	Nd II
He I	2.4	4.8	15.3	18.0	24.5
He II	6.0	10.6	37.3	44.5	47.5
Sr II	2.5	5.7	16.5	19.1	20.6
Xe II	1.1	2.4	7.1	8.2	8.8
Nd II	1.3	3.6	9.3	10.6	11.4

**Table 2.** Work per ion pair for beta decay for various target ions and media. The values presented are in units of  $I$ , the first ionization potential for the given ionization state. We adopt  $\chi_e = 0.1$  for He I and  $\chi_e = 1$  otherwise.

Using the electron spectra, we compute the work per ion pair,  $w$ , for Xe ions. Figure 5 (*right*) shows  $w/I$ , where  $I$  is the first ionization potential of the target ion. For Xe ions, the values  $w/I$  for different ionization stages are roughly the same for a given  $\chi_e$  and increase with increasing  $\chi_e$ . These results are quantitatively similar to those obtained for alpha decay and fission (see Table 1a). We also note that, among heavy-ion species, the work per ion pair scales with the effective number of electrons in the target ion, as discussed in Appendix B. This scaling can be used to estimate approximate values of the work per ion pair for various ion species.

## 5 DISCUSSION

In this section, we discuss our findings on the heating and ionization caused by fission fragments and alpha decay particles. These results will be compared to the ionization efficiencies and spectra found for  $\beta$ -electrons.

Figure 1 shows that the late-time heating rate follows power-law behaviour. Specifically, the fission heating rate scales as  $\dot{q}_{\text{fis}} \propto t^{-3}$  for  $t \approx \tau_{\text{fis}}$ , transitions to  $\dot{q}_{\text{fis}} \propto t^{-5}$  for  $t \gg \tau_{\text{fis}}$ , and for alpha decay, we find  $\dot{q}_\alpha \propto t^{-2.8}$ . This behaviour arises from the approximately constant number of decays over time in a decay chain. As the material expands adiabatically, its density evolves as  $\rho_m(t) \propto t^{-3}$ , which sets the baseline for the heating rate. The energy dependence of the stopping cross section modifies this to  $t^{-2.8}$ , while the adiabatic expansion in the case of fission further steepens the decline to  $t^{-5}$ .

This heating-rate prescription remains consistent with Hotokezaka

& Nakar (2020), even though we adopt a different stopping-power formulation to ensure self-consistent thermalization and ionization.

In all three presented cases for the work per ion pair values, as the ambient material becomes more highly ionized, the ionization efficiency of the projectile naturally decreases. When a quasi-neutral single species ejecta is assumed as above, each increase in ionization state for the plasma ions will increase the number of thermal electrons while also leaving fewer bound electrons available for further ionization. Higher charge states also have more tightly bound outer electrons, making additional ionization progressively harder, though the effect of this is rather small for heavier elements such as xenon. For Xe II, the bound- and free-electron stopping powers at the injection energies of both fission fragments and  $\alpha$ -particles are already comparable, reducing the ionization efficiency by roughly a factor of two relative to Xe I. This demonstrates that most ionizations occur while the projectile is still near its initial, highest velocity. The similar values for the stopping cross sections of Xe II and the thermal electrons further suggest a scaling relation: although xenon ions in these charge states still retain many loosely bound electrons, the number of thermal electrons increases with each ionization stage, leading to the approximate scaling

$$\text{WIP} \approx \text{WIP}_{\chi_e=1} \times \left( \frac{\chi_e + 1}{2} \right),$$

where  $\text{WIP}_{\chi_e=1}$  is the work per ion pair for the case where  $\chi_e = 1$ .

As noted in Section 4, the ionization efficiencies of fission fragments and  $\alpha$ -particles closely resemble those of  $\beta$ -electrons (see Tables 1b and 2). This similarity is most pronounced for heavier ionization targets such as Sr II, Xe II, and Nd II, whose fuller and more complex electron shells provide many loosely bound outer electrons (see also Appendix B). In contrast, for He I–II the ionization efficiency differs by a factor of a few. This arises from the larger binding energies and the limited number of outer-shell electrons available to fission fragments and  $\alpha$ -particles, an effect that is less significant for the  $\beta$ -electron ionization cross sections and therefore produces the observed discrepancy.

## 6 CONCLUSION

In this work, ionization and thermalization by  $\alpha$ -particles and spontaneous-fission fragments in kilonova ejecta were studied self-consistently, including stopping powers, particle spectra, charge evolution, and interactions with bound and free electrons. Corresponding calculations for  $\beta$ -electrons were also performed to compare the ionization efficiencies of the different radioactive decay channels.

The main result is that the work per ion pair is remarkably robust across all considered decay products. Despite the large differences in particle mass, charge, and injection energy between  $\beta$ -electrons,  $\alpha$ -particles, and fission fragments, the resulting ionization efficiencies are found to be quantitatively very similar, particularly for heavy-element ejecta compositions relevant to kilonovae. This behaviour follows from the common collision physics governing both stopping and ionization, which causes the ratio between ionization and energy loss to remain approximately constant over the relevant energy range and ejecta compositions.

These results suggest that the late-time ionization state of kilonova ejecta depends only weakly on which radioactive decay channel dominates the heating, even in ejecta enriched by actinides where  $\alpha$ -decay and fission become important.

## ACKNOWLEDGEMENTS

We thank Dr Tanja Hinderer for useful discussion. This work was supported by the JST FOREST Program (JPMJFR2136) and the JSPS Grant-in-Aid for Scientific Research (23H01169, 23H04900).

## DATA AVAILABILITY

The data underlying this article will be shared on reasonable request to the corresponding authors.

## REFERENCES

- Alpher R. A., Bethe H., Gamow G., 1948, *Phys. Rev.*, 73, 803  
 Arya A., Damgaard R., Sneppen A., Dougan D. J., Sim S. A., Ballance C. P., Watson D., 2026, *arXiv e-prints*, p. [arXiv:2604.05812](https://arxiv.org/abs/2604.05812)  
 Axelrod T. S., 1980, Ph.D. thesis, University of California Santa Cruz, Santa Cruz, United States  
 Baek W. Y., Grosswendt B., 1995, *Phys. Med. Biol.*, 40, 1015  
 Bar-Shalom A., Klapisch M., Oreg J., 2001, *Journal of Quantitative Spectroscopy and Radiative Transfer*, 71, 169  
 Barnes J., Kasen D., Wu M.-R., Martínez-Pinedo G., 2016, *The Astrophysical Journal*, 829, 110  
 Bartos I., Marka S., 2019, *Nature*, 569, 85  
 Bateman H., 1910, in *Proceedings of the Cambridge Philosophical Society*, pp 423–427  
 Berger M. J., Coursey J. S., Zucker M. A., Chang J., 2005, ESTAR, PSTAR, and ASTAR: Computer Programs for Calculating Stopping-Power and Range Tables for Electrons, Protons, and Helium Ions (version 1.2.3), <https://physics.nist.gov/PhysRefData/Star/Text/ASTAR.html>  
 Bohr N., 1913, *The London, Edinburgh, and Dublin Philosophical Magazine and Journal of Science*, 25, 10  
 Brethauer D., Kasen D., Margutti R., Chornock R., 2026, *ApJ*, 996, 64  
 Burbidge E. M., Burbidge G. R., Fowler W. A., Hoyle F., 1957, *Reviews of Modern Physics*, 29, 547  
 Burris D. L., Pilachowski C. A., Armandroff T. E., Sneden C., Cowan J. J., Roe H., 2000, *The Astrophysical Journal*, 544, 302–319

- Cameron A. G., 1957, Technical report, Stellar evolution, nuclear astrophysics, and nucleogenesis. Second edition, <https://www.osti.gov/biblio/4709881>. Atomic Energy of Canada Ltd., Chalk River, Ontario (Canada), <https://www.osti.gov/biblio/4709881>  
 Chiba K., Tanaka M., Wanajo S., Fujibayashi S., Kawaguchi K., Hotokezaka K., 2026, *arXiv e-prints*, p. [arXiv:2604.05703](https://arxiv.org/abs/2604.05703)  
 Chiesa L., Perego A., Guercilena F. M., 2024, *ApJ*, 962, L24  
 Côté B., Lugaro M., Reifarth R., Pignatari M., Világos B., Yagüe A., Gibson B. K., 2019, *ApJ*, 878, 156  
 Domoto N., Tanaka M., Kato D., Kawaguchi K., Hotokezaka K., Wanajo S., 2022, Lanthanide Features in Near-infrared Spectra of Kilonovae ([arXiv:2206.04232](https://arxiv.org/abs/2206.04232)), <https://arxiv.org/abs/2206.04232>  
 Fujibayashi S., Kiuchi K., Wanajo S., Kyutoku K., Sekiguchi Y., Shibata M., 2023, *ApJ*, 942, 39  
 Gamow G., 1928, *Zeitschrift für Physik*, 51, 204–212  
 Giesen U., Beck J., 2014, *Radiat. Prot. Dosimetry*, 161, 23  
 Gryziński M., 1965a, *Phys. Rev.*, 138, A305  
 Gryziński M., 1965b, *Phys. Rev.*, 138, A322  
 Gryziński M., 1965c, *Phys. Rev.*, 138, A336  
 Holmbeck E. M., Barnes J., Lund K. A., Sprouse T. M., McLaughlin G. C., Mumpower M. R., 2023, *The Astrophysical Journal Letters*, 951, L13  
 Hotokezaka K., Nakar E., 2020, *The Astrophysical Journal*, 891, 152  
 Hotokezaka K., Piran T., Paul M., 2015, *Nature Physics*, 11, 1042  
 Hotokezaka K., Wanajo S., Tanaka M., Bamba A., Terada Y., Piran T., 2016, *MNRAS*, 459, 35  
 Hotokezaka K., Tanaka M., Kato D., Gaigalas G., 2021, *Monthly Notices of the Royal Astronomical Society*  
 Hotokezaka K., Tanaka M., Kato D., Gaigalas G., 2023, Tellurium emission line in kilonova AT 2017gfo ([arXiv:2307.00988](https://arxiv.org/abs/2307.00988)), <https://arxiv.org/abs/2307.00988>  
 International Atomic Energy Agency 2025, LiveChart of Nuclides, <https://www-nds.iaea.org/relnsd/vcharthtml/VChartHTML.html>  
 Jerkstrand A., et al., 2026, *MNRAS*, 548, stag733  
 Kasen D., Barnes J., 2019, *ApJ*, 876, 128  
 Kasen D., Metzger B., Barnes J., Quataert E., Ramirez-Ruiz E., 2017, *Nature*, 551, 80–84  
 Kawaguchi K., Domoto N., Fujibayashi S., Hamidani H., Hayashi K., Shibata M., Tanaka M., Wanajo S., 2024, Three dimensional end-to-end simulation for kilonova emission from a black-hole neutron-star merger ([arXiv:2404.15027](https://arxiv.org/abs/2404.15027)), <https://arxiv.org/abs/2404.15027>  
 Kozma C., Fransson C., 1992, *ApJ*, 390, 602  
 Lattimer J. M., Schramm D. N., 1974, *ApJ*, 192, L145  
 McGuire J. H., Richard P., 1973, *Phys. Rev. A*, 8, 1374  
 Mulholland L. P., Ramsbottom C. A., Ballance C. P., Sneppen A., Sim S. A., 2026, *MNRAS*, 546, stag237  
 Opal C. B., Peterson W. K., Beaty E. C., 1971, *J. Chem. Phys.*, 55, 4100  
 Peebles P. J., 1966, *Phys. Rev. Lett.*, 16, 410  
 Peter T., Meyer-ter Vehn J., 1991a, *Phys. Rev. A*, 43, 1998  
 Peter T., Meyer-ter Vehn J., 1991b, *Phys. Rev. A*, 43, 2015  
 Pognan Q., Grumer J., Jerkstrand A., Wanajo S., 2023, *MNRAS*, 526, 5220  
 Radice D., Perego A., Hotokezaka K., Fromm S. A., Bernuzzi S., Roberts L. F., 2018, *ApJ*, 869, 130  
 Schiwietz G., Grande P., 2001, *Nuclear Instruments and Methods in Physics Research Section B: Beam Interactions with Materials and Atoms*, 175–177, 125  
 Sneppen A., Watson D., 2023, *Astronomy & Astrophysics*, 675, A194  
 Sneppen A., Watson D., Damgaard R., Heintz K. E., Vieira N., Väisänen P., Mahoro A., 2024a, *A&A*, 690, A398  
 Sneppen A., Damgaard R., Watson D., Collins C. E., Shingles L., Sim S. A., 2024b, *A&A*, 692, A134  
 Spencer L. V., Fano U., 1954, *Phys. Rev.*, 93, 1172  
 Sun Q., et al., 2018, *WIREs Computational Molecular Science*, 8, e1340  
 Tanaka M., et al., 2018, *ApJ*, 852, 109  
 Tanaka M., et al., 2023, *The Astrophysical Journal*, 953, 17  
 Tarumi Y., Hotokezaka K., Domoto N., Tanaka M., 2023, *arXiv e-prints*, p. [arXiv:2302.13061](https://arxiv.org/abs/2302.13061)  
 Tissot F. L. H., Dauphas N., Grossman L., 2016, *Science Advances*, 2, e1501400

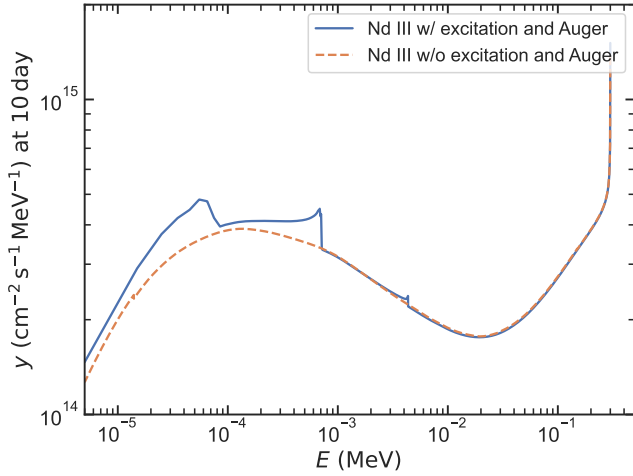


**Figure A1.** Electron degradation spectrum with and without electron impact excitation and Auger electrons for Nd III medium.

- Wagoner R. V., Fowler W. A., Hoyle F., 1967, *ApJ*, 148, 3  
 Wallner A., et al., 2015, *Nature Communications*, 6, 5956  
 Wallner A., et al., 2021, *Science*, 372, 742  
 Wanajo S., 2018, *ApJ*, 868, 65  
 Watson D., et al., 2019, *Nature*, 574, 497  
 Waxman E., Ofek E. O., Kushnir D., 2019, *ApJ*, 878, 93  
 Wehmeyer B., López A. Y., Côté B., K. Pető M., Kobayashi C., Lugaro M., 2023, *ApJ*, 944, 121  
 Wu M.-R., Barnes J., Martínez-Pinedo G., Metzger B. D., 2019a, *Phys. Rev. Lett.*, 122, 062701  
 Wu M.-R., Barnes J., Martínez-Pinedo G., Metzger B. D., 2019b, *Phys. Rev. Lett.*, 122, 062701  
 Zhu Y., et al., 2018, *The Astrophysical Journal Letters*, 863, L23

## APPENDIX A: EFFECTS OF EXCITATION AND AUGER ELECTRONS ON ELECTRON DEGRADATION SPECTRUM

In this work, we do not account for stopping due to excitation and for the contribution of Auger electrons in the electron degradation spectrum (equation 29). To assess the impact of this simplification, we compute the degradation spectrum of  $\beta$  electrons in Nd III medium with  $\chi_e = 2$  including both effects. The excitation cross sections and Auger rates are computed using HULLAC. Figure A1 shows the degradation spectra computed with and without these effects. We find that they are identical down to  $\sim 1$  keV. At lower energies, Auger electrons enhance the degradation spectrum by up to  $\approx 10\%$ . Similarly, the work per ion pair is expected to increase by only  $\mathcal{O}(10\%)$ . Therefore, we conclude that neglecting excitation and Auger electrons does not significantly affect the ionization efficiencies in kilonova plasma.

## APPENDIX B: ANALYTIC SCALING FOR WORK PER ION PAIR

We show a simple analytic estimate for the work per ion pair by considering how the ionization rate depends on the atomic structure of the stopping medium. For a given degradation spectrum,  $y(E)$ ,

the production rate of electron-ion pairs is

$$\mathcal{N}_i \propto \sum_j \int_{I_j}^{E_0} dE \sigma_{\text{ion},j}(E) y(E), \quad (\text{B1})$$

where the summation is over atomic shells. where  $\sigma_{\text{ion},j}(E)$  is the ionization cross section for a shell  $j$  with  $N_j$  electrons:

$$\sigma_{\text{ion},j}(E) \propto \frac{N_j \ln(E/I_j)}{I_j E}. \quad (\text{B2})$$

Therefore,

$$\mathcal{N}_i \propto \sum_j \frac{N_j}{I_j} \int_{I_j}^{E_0} dE \frac{y(E) \ln(E/I_j)}{E}. \quad (\text{B3})$$

The integral part is only weakly dependent on  $I_j$  and the injection energy  $E_0$ , and thus, we obtain

$$\mathcal{N}_i \propto \sum_j \frac{N_j}{I_j}. \quad (\text{B4})$$

Using this, the work per ion pair is inversely proportional to the number of electrons weighted by the potential energies of shells

$$\text{WIP} \propto \left( \sum_j \frac{I_0}{I_j} N_j \right)^{-1}. \quad (\text{B5})$$

This approximate scaling enables the computation of the work per ion pair for various ion species for a given  $y(E)$ .

This paper has been typeset from a  $\text{\LaTeX}$  file prepared by the author.